RESEARCH ARTICLE

Performance analysis and material distribution optimization for sound barriers using a semianalytical meshless method

Hanqing Liu[1] | Fajie Wang[1] | Chuanzeng Zhang[2]

[1]National Engineering Research Center for Intelligent Electrical Vehicle Power System, College of Mechanical and Electrical Engineering, Qingdao University, Qingdao, China

[2]Department of Civil Engineering, University of Siegen, Siegen, Germany

Correspondence
Prof. Fajie Wang, National Engineering Research Center for Intelligent Electrical Vehicle Power System, College of Mechanical and Electrical Engineering, Qingdao University, Qingdao, China.
Email: wfj88@qdu.edu.cn

Prof. Chuanzeng Zhang, Department of Civil Engineering, University of Siegen, Siegen, Germany.
Email: c.zhang@uni-siegen.de

Abstract

With the increase in car ownership, traffic noise pollution has increased considerably and is one of the most severe types of noise pollution that affects living standards. Noise reduction by sound barriers is a common protective measure used in this country and abroad. The acoustic performance of a sound barrier is highly dependent on its shape and material. In this paper, a semianalytical meshless Burton–Miller-type singular boundary method is proposed to analyze the acoustic performance of various shapes of sound barriers, and the distribution of sound-absorbing materials on the surface of sound barriers is optimized by combining a solid isotropic material with a penalization method. The acoustic effect of the sound-absorbing material is simplified as the acoustical impedance boundary condition. The objective of optimization is to minimize the sound pressure in a given reference plane. The volume of the sound-absorbing material is used as a constraint. The density of the nodes covered with the sound-absorbing material is used as the design variable. The method of moving asymptotes was used to update the design variables. This model completely avoids the mesh discretization process in the finite element method and requires only boundary nodes. In addition, the approach also does not require the singular integral calculation in the boundary element method. The method is illustrated and validated using numerical examples to demonstrate its accuracy and efficiency.

KEYWORDS
sound barrier, acoustic analysis, material distribution optimization, semianalytical meshless method

1 | INTRODUCTION

While the rapid development of transportation has provided convenience and comfort in terms of travel, noise pollution has also accordingly increased considerably. Long-term exposure to traffic noise can lead to adverse health effects, including insomnia, hypertension, and cardiovascular disease. Consequently, the implementation of sound barriers has become a common practice in mitigating the noise impact caused by traffic. Over the past few decades, both domestically and internationally, researchers have shown sustained interest in enhancing the acoustic performance of sound barriers. The geometry and material composition are the primary factors influencing the acoustic performance of sound barriers. Traditionally, sound barriers are designed based on experimental testing. May and Osman[1] investigated the acoustic performance of different shapes of sound barriers. Joynt and Kang[2]

and Hong and Jeon[3] evaluated the effect of various materials on the sound barrier.

The direct experimental evaluation of sound barriers is costly, time-consuming, inflexible, and limited in terms of variable control. With advancements in computational techniques and numerical methods, simulation-based approaches have gained prominence in designing and optimizing sound barriers. Various numerical methods have been developed, including the finite element method (FEM)[4,5] and the boundary element method (BEM).[6,7] Reiter et al.[4] developed a periodic FEM model to calculate the sound reflection properties of any layered acoustic system. Papadakis and Stavroulakis[5] accurately estimated the insertion loss of sound barriers by utilizing FEM. Monazzam et al.[6] investigated the performance of T-shaped sound barriers covered with oblique diffusers using the BEM. Additionally, Lam[7] predicted the insertion loss of sound barriers in the presence of atmospheric turbulence using BEM.

Previous studies have predominantly focused on the shape optimization of sound barriers. Grubeša et al.[8] utilized BEM and genetic algorithms to optimize the structure of the sound barrier. Liu et al.[9] and Chen et al.[10] optimized the shape of the sound barrier by using isogeometric BEM. Desai et al.[11] introduced the level-set method to optimize sound barriers topologically. Recently, increased attention has been focused in research on optimizing the distribution of sound-absorbing materials. Kim and Yoon[12] combined FEM and a gradient-based optimizer to optimize the distribution of rigid and sound-absorbing materials. Zhao et al.[13] and Chen et al.[14] optimized the distribution of sound-absorbing materials at the edge of the sound barrier by integrating BEM with an optimality criteria (OC) solver. It is undeniable that FEM and BEM have achieved great success. However, they involve cumbersome mesh generation and singular integral calculation.

In recent years, many efforts have been devoted to the development of various meshless methods[15–24] to avoid mesh generation in FEM and singular integral calculation in BEM. A more detailed background on meshless methods can be found in Refs. [25–27]. Among them, the Burton–Miller-type singular boundary method (BM-SBM) proposed by Fu et al.[28] is a semianalytical and boundary-type meshless scheme, and has been successfully applied to high-frequency acoustic radiation and scattering,[29] acoustic design sensitivity analysis,[30,31] and spurious eigensolutions in exterior acoustic problems.[32]

In this study, BM-SBM is utilized to analyze the acoustic performance of sound barriers with different shapes. The influence of the distribution of sound-absorbing materials on the acoustic performance of sound barriers is discussed. Finally, the distribution of sound-absorbing materials on the surface of the sound barrier is optimized using the method of moving asymptotes (MMA).[33] The solid isotropic material with penalization (SIMP)[34] technique is used to force the solution rapidly to approach 0 or 1, where 0 and 1 denote the void and the material, respectively. Although the SIMP method can eliminate intermediate densities, some intermediate-density elements still exist in actual optimization. Therefore, the volume-preserving nonlinear density filter[35] based on the Heaviside function is introduced to suppress the intermediate density.

The rest of the paper is structured as follows: The governing equations and the fundamental solutions are presented in Section 2.

Section 3 describes BM-SBM for acoustic radiation and scattering problems. Section 4 presents a topological optimization model for the distribution of sound-absorbing material on the sound barrier. Section 5 presents several numerical tests to establish the validity and accuracy of the proposed optimization method. Finally, the paper is summarized with some concluding remarks in Section 6.

2 | PROBLEM STATEMENT

2.1 | Governing equation and boundary conditions

Consider the sound propagation in a homogeneous isotropic medium; the governing equation for an exterior acoustic problem can be written as

$$(\nabla^2 + k^2)p(\mathbf{x}) = 0 \quad \mathbf{x} \in \Omega, \tag{1}$$

where ∇^2 represents the Laplacian operator, $k = \omega/c$ is the acoustic wavenumber, with ω being the angular frequency and c being the sound wave speed in the medium, and $p(\mathbf{x})$ denotes the sound pressure at the point $\mathbf{x}$ inside the acoustic domain Ω.

The boundary conditions of acoustic problems can be categorized into three types as follows:

The Dirichlet boundary condition

$$p(\mathbf{x}) = \bar{p}(\mathbf{x}), \quad \mathbf{x} \in \Gamma_D, \tag{2}$$

the Neumann boundary condition

$$\frac{\partial p(\mathbf{x})}{\partial n_{\mathbf{x}}} = i\rho\omega\bar{v}(\mathbf{x}), \quad \mathbf{x} \in \Gamma_N, \tag{3}$$

and the impedance boundary condition

$$\frac{\partial p(\mathbf{x})}{\partial n_{\mathbf{x}}} = ik\beta(\mathbf{x})p(\mathbf{x}), \quad \mathbf{x} \in \Gamma_I, \tag{4}$$

where $\bar{p}(\mathbf{x})$ is the known sound pressure, $\bar{v}(\mathbf{x})$ is the known normal velocity, i is the imaginary unit, ρ is the density of the medium, and $\beta(\mathbf{x})$ represents the surface admittance at position $\mathbf{x}$.

For the exterior acoustic problem, the sound pressure $p(\mathbf{x})$ at the infinite field should satisfy the Sommerfeld radiation condition:

$$\lim_{r \to \infty} \left(\sqrt{r} \left(\frac{\partial p(\mathbf{x})}{\partial r} - ikp(\mathbf{x}) \right) \right) = 0, \tag{5}$$

where r is the distance from the point $\mathbf{x}$ to the center of the sound field.

2.2 | Fundamental solutions

The fundamental solutions of the two-dimensional (2D) Helmholtz equation are expressed as

$$G(\mathbf{x}, s) = \frac{i}{4}H_0^{(1)}(kr), \tag{6}$$

$$\frac{\partial G(\boldsymbol{x}, \boldsymbol{s})}{\partial n_{\boldsymbol{x}}} = -\frac{\mathrm{i}k}{4r} H_1^{(1)}(kr)((x_1 - s_1)n_{x1} + (x_2 - s_2)n_{x2}), \qquad (7)$$

where $\boldsymbol{x}$ and $\boldsymbol{s}$ are the field and source points, respectively. $r = \|\boldsymbol{x} - \boldsymbol{s}\|_2$ is the Euclidean distance between points $\boldsymbol{x}$ and $\boldsymbol{s}$. x_i, s_i, and n_{x_i} are Cartesian components of point $\boldsymbol{x}$, point $\boldsymbol{s}$, and normal vector $\boldsymbol{n_x}$, respectively. $H_0^{(1)}$ is the zero-order Hankel function of the first kind. The derivative of the m-order Hankel function of the first kind satisfies the following rule:

$$\left[H_m^{(1)}(t) \right]' = \frac{m}{t} \left[H_m^{(1)}(t) \right] - \left[H_{m+1}^{(1)}(t) \right]. \qquad (8)$$

In a 2D problem with a half-space, the fundamental solutions can be written as

$$G(\boldsymbol{x}, \boldsymbol{s}) = \frac{\mathrm{i}}{4} H_0^{(1)}(kr) + \frac{\mathrm{i}}{4} H_0^{(1)}(kr'), \qquad (9)$$

$$\frac{\partial G(\boldsymbol{x}, \boldsymbol{s})}{\partial n_{\boldsymbol{x}}} = -\frac{\mathrm{i}k}{4} \left\{ \frac{1}{r} H_1^{(1)}(kr)[(x_1 - s_1)n_{x1} + (x_2 - s_2)n_{x2}] \right. \\ \left. + \frac{1}{r'} H_1^{(1)}(kr')[(x_1 - s_1')n_{x1} + (x_2 - s_2')n_{x2}] \right\}, \qquad (10)$$

where $\boldsymbol{s}'$ is the image point of source point $\boldsymbol{s}$ with respect to the ground, $r' = \|\boldsymbol{x} - \boldsymbol{s}'\|_2$.

3 | NUMERICAL METHODOLOGY

3.1 | BM-SBM formulation for 2D acoustic problems

BM-SBM is a boundary-type meshless method. In BM-SBM, N collocation points are placed on the physical boundary to coincide with the source points (Figure 1), and the solution of the Helmholtz equation can be approximated by a linear combination of the fundamental solutions:
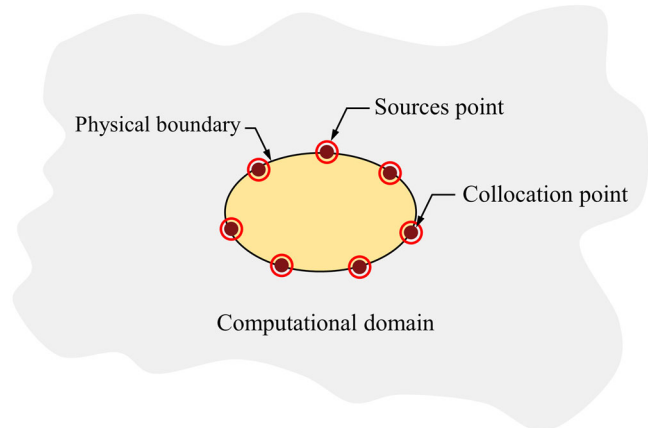
FIGURE 1 Schematic diagram of the distributions of sources and collocation points in BM-SBM for exterior problems.

$$p(\boldsymbol{x}_i) = \sum_{\substack{j=1 \\ i \neq j}}^{N} \alpha_j(G(\boldsymbol{x}_i, \boldsymbol{s}_j) + \lambda E(\boldsymbol{x}_i, \boldsymbol{s}_j)) + \alpha_i h_{ii}^{BM}, \quad \boldsymbol{x}_i \in \Gamma_D, \boldsymbol{s}_j \in \Gamma, \qquad (11)$$

$$\frac{\partial p(\boldsymbol{x}_i)}{\partial n_{\boldsymbol{x}}} = \sum_{\substack{j=1 \\ i \neq j}}^{N} \alpha_j(M(\boldsymbol{x}_i, \boldsymbol{s}_j) + \lambda H(\boldsymbol{x}_i, \boldsymbol{s}_j)) + \alpha_i q_{ii}^{BM}, \quad \boldsymbol{x}_i \in \Gamma_N, \boldsymbol{s}_j \in \Gamma, \qquad (12)$$

$$\frac{\partial p(\boldsymbol{x}_i)}{\partial n_{\boldsymbol{x}}} - \mathrm{i}k\beta(\boldsymbol{x}_i)p(\boldsymbol{x}_i) = \sum_{\substack{j=1 \\ i \neq j}}^{N} \alpha_j(M(\boldsymbol{x}_i, \boldsymbol{s}_j) + \lambda H(\boldsymbol{x}_i, \boldsymbol{s}_j)) + \alpha_i q_{ii}^{BM} \\ - \mathrm{i}k \left(\sum_{\substack{j=1 \\ i \neq j}}^{N} \beta(\boldsymbol{x}_i)\alpha_j(G(\boldsymbol{x}_i, \boldsymbol{s}_j) + \lambda E(\boldsymbol{x}_i, \boldsymbol{s}_j)) + \beta(\boldsymbol{x}_i)\alpha_i h_{ii}^{BM} \right), \\ \boldsymbol{x}_i \in \Gamma_I, \boldsymbol{s}_j \in \Gamma, \qquad (13)$$

where $M(\boldsymbol{x}_i, \boldsymbol{s}_j) = \frac{\partial G(\boldsymbol{x}_i, \boldsymbol{s}_j)}{\partial n_{x_i}}$, $E(\boldsymbol{x}_i, \boldsymbol{s}_j) = \frac{\partial G(\boldsymbol{x}_i, \boldsymbol{s}_j)}{\partial n_{s_i}}$, $H(\boldsymbol{x}_i, \boldsymbol{s}_j) = \frac{\partial^2 G(\boldsymbol{x}_i, \boldsymbol{s}_j)}{\partial n_{x_j} \partial n_{x_i}}$, $\lambda = \frac{\mathrm{i}}{k+1}$, N represents the number of the nodes and h_{ii}^{BM} and q_{ii}^{BM} are the origin intensity factors (OIFs) corresponding to the Burton–Miller-type formulations. $\{\alpha_j\}_{j=1,\dots,N}$ are the unknown coefficients. Equation (13) can be considered as a linear combination of Equations (11) and (12).

Using Equations (11)–(13) and matching with the boundary conditions in Equations (2)–(4), a linear system can be obtained:

$$\boldsymbol{A}\boldsymbol{\alpha} = \boldsymbol{b}, \qquad (14)$$

where $\boldsymbol{A}$ denotes the coefficient matrix, $\boldsymbol{b}$ represents the boundary conditions, and $\boldsymbol{\alpha}$ is the unknown coefficient. It can be found that the matrix $\boldsymbol{A}$ and the vector $\boldsymbol{b}$ are available. Once the unknown coefficient $\boldsymbol{\alpha}$ is computed, the sound pressure $p(\boldsymbol{x})$ at any point inside the domain can be calculated by

$$p(\boldsymbol{x}) = \sum_{j=1}^{N} \alpha_j(G(\boldsymbol{x}, \boldsymbol{s}_j) + \lambda E(\boldsymbol{x}, \boldsymbol{s}_j)), \quad \boldsymbol{x} \in \Omega, \boldsymbol{s}_j \in \Gamma. \qquad (15)$$

3.2 | OIFs

OIFs are a key problem for BM-SBM. There are several methods to calculate the OIFs, such as the subtraction and adding-back technique (SAB), the inverse interpolation technique, and empirical formulas. In this work, SAB and empirical formulas are used to calculate h_{ii}^{BM} and q_{ii}^{BM}:

$$h_{ii}^{BM} = h_{ii} - \lambda \sum_{\substack{j=1 \\ i \neq j}}^{N} \frac{L_j}{L_i} \frac{\partial G_0(\boldsymbol{x}_i, \boldsymbol{s}_j)}{\partial n_{s_j}}, \qquad (16)$$

$$q_{ii}^{BM} = q_{ii} + \lambda \left(\frac{k^2}{2} h_{ii} - \sum_{\substack{j=1 \\ i \neq j}}^{N} \frac{L_j}{L_i} \frac{\partial^2 G_0(\boldsymbol{x}_i, \boldsymbol{s}_j)}{\partial n_{s_j} \partial n_{x_i}} \right), \qquad (17)$$

where L_j is the half-length of the curve between the source points $\boldsymbol{s}_{j-1}$ and $\boldsymbol{s}_{j+1}$ on the physical boundary as shown in Figure 2, $G_0(\boldsymbol{x}_i, \boldsymbol{s}_j) = -\ln \|\boldsymbol{x}_i - \boldsymbol{s}_j\|_2 / 2\pi$, h_{ii} and q_{ii} can be calculated as follows:
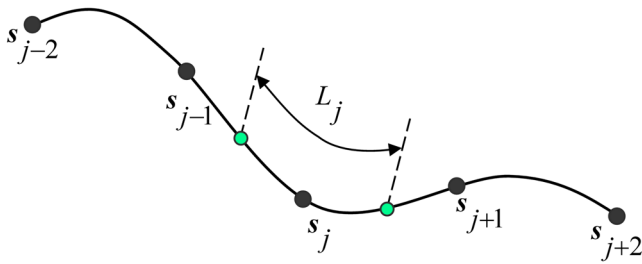
FIGURE 2 Schematic configuration of the source points s_j and the curve L_j.

$$h_{ii} = \frac{i}{4} - \frac{1}{2\pi}\left(\ln\left(\frac{L_i}{2\pi}\right) + \ln\left(\frac{k}{2}\right) + \gamma \right), \quad (18)$$

$$q_{ii} = \frac{1}{L_i} - \sum_{\substack{j=1 \\ i \neq j}}^{N} \frac{L_j}{L_i} \frac{\partial G_0(x_i, s_j)}{\partial n_{s_j}}, \quad (19)$$

where γ is the Euler–Mascheroni constant.

4 | TOPOLOGY OPTIMIZATION MODEL WITH BM-SBM

4.1 | Optimization model

A sound-absorbing material is designed to absorb sound energy and reduce sound reflection. Its working principle is shown in Figure 3. This paper aims to improve the sound insulation properties of the sound barrier by optimizing the distribution of the sound-absorbing material. In this study, the optimization problem can be formulated as follows:

$$\begin{cases} \underset{\rho}{\text{Minimize:}} \quad \Pi = p_f^H p_f, \\ \text{Subject to :} \quad \sum_{i=1}^{N_e} \rho_i v_i - \xi \sum_{i=1}^{N_e} v_i \leq 0 \\ \quad 0 \leq \rho_{min} \leq \rho_i \leq 1, i = 1, 2, ..., N_e, \end{cases} \quad (20)$$

where the objective function is the minimization of sound pressure, p_f denotes the sound pressure vector in the field points located on a prescribed reference plane, p_f^H denotes the conjugate transpose of p_f, $\rho_i(i = 1, 2, ..., N_e)$ denotes the ith design variable of the relative material density, with N_e being the total number of design variables, v_i is the volume corresponding to nodes, ξ is the volume fraction ratio constraint, and ρ_{min} is a small positive value to avoid the singularity of the matrix, for example, ρ_{min} = 0.000 1.

The SIMP method is introduced into the material distribution optimization problem. The relationship between β_i and ρ_i is expressed as

$$\beta_i = \beta_0 f(\rho_i), \quad (21)$$

where β_0 is the normalized surface admittance value. The SIMP interpolation function is introduced as

$$f(\rho_i) = \rho_i^{\eta}, \quad (22)$$
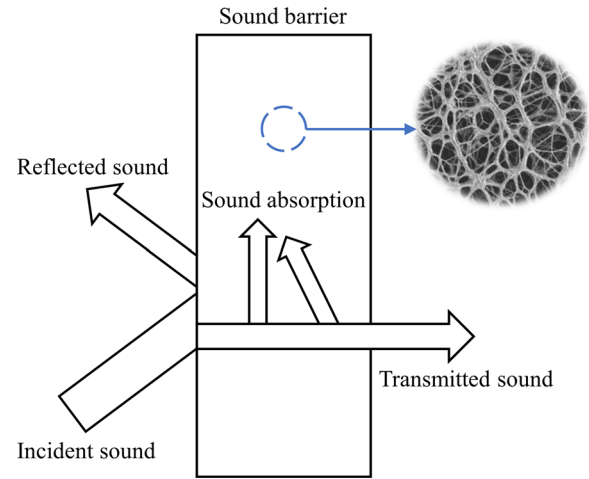
FIGURE 3 Sound absorption diagram of porous materials.

where the penalization parameter η = 3 is recommended in this work. The η can eliminate intermediate densities, causing them to rapidly approach 0 or 1, where 0 and 1 denote the void and the material, respectively. Although the SIMP method can eliminate intermediate densities, some intermediate-density elements still exist in actual optimization. Therefore, we introduced a volume-preserving nonlinear density filter to suppress the intermediate density.

4.2 | Acoustic sensitivity with respect to the design variable

The optimization problem is solved by a gradient-based mathematical programming algorithm, which requires a sensitivity analysis of the objective function with respect to the design variables. The sensitivity of the objective function with respect to the design variable $\rho_i(i = 1, 2, ..., N_e)$ is

$$\frac{\partial \Pi}{\partial \rho_i} = 2\Re\left(p_f^H \frac{\partial p_f}{\partial \rho_i} \right). \quad (23)$$

By differentiating Equation (15) with respect to the design variable ρ, the design sensitivity can be derived as follows:

$$\frac{\partial p(x)}{\partial \rho_i} = \sum_{j=1}^{N} \left[\frac{\partial \alpha_j}{\partial \rho_i}(G(x, s_j) + \lambda E(x, s_j)) + \alpha_j \frac{\partial(G(x, s_j) + \lambda E(x, s_j))}{\partial \rho_i} \right], \quad (24)$$

in which fundamental solutions are designed to be variable-independent, so they are zero relative to the derivative of ρ_i; $\frac{\partial \alpha_j}{\partial \rho_i}$ can be calculated using the adjoint variable method.[36]

4.3 | Design variable update criteria

In this work, MMA is used to solve optimization problems. The convergence rule is given as follows:
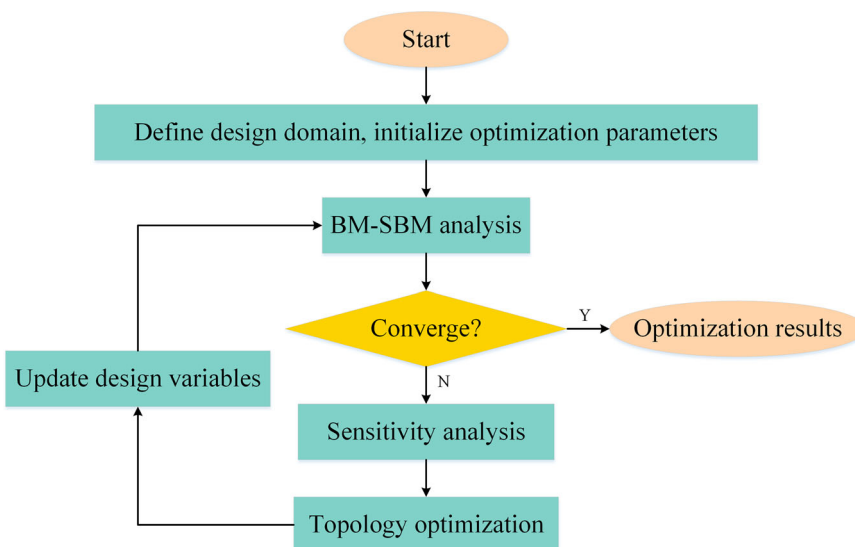
WILEY

FIGURE 4 Flowchart of topology optimization.

$$\left| \frac{\Pi_{\psi+1} - \Pi_{\psi}}{\Pi_{\psi}} \right| \leq \tau, \tag{25}$$

where τ is the convergence parameter. The flowchart of topology optimization is shown in Figure 4.

5 | NUMERICAL RESULTS AND DISCUSSION

Three numerical examples are used to study the acoustic performance analysis of sound barrier and topology optimization of sound-absorbing material distribution. The first example discusses the acoustic performance of three sound barriers. In Example 2, the insertion loss of the sound barrier in five cases is considered. Finally, in Example 3, the topology optimization of sound-absorbing material distribution is studied.

According to research, urban traffic noise is mainly composed of low-frequency and mid-frequency noise. Table 1 shows the main frequencies of the different roads.[37] In the simulation, the center frequencies of the main frequencies of the three roads are used as the test frequencies. The medium of the acoustic field is assumed to be air with the following parameters: the density is $\rho = 1.2$ kg/m^3, and the sound velocity is $c = 340$ m/s. The reference sound pressure is $p_{ref} = 2.0 \times 10^{-5}$ Pa. The sound pressure level (SPL) is calculated from

$$SPL = 20 \log_{10} \frac{|p|}{p_{ref}}. \tag{26}$$

The noise reduction effect of the sound barrier can be measured by the insertion loss as follows:

$$IL = 20 \log_{10} \left| \frac{p_0}{p} \right|, \tag{27}$$

TABLE 1 Main frequencies of different roads.

| Type of roads	Flat and straight roads	Elevated roads	Tunnel
Main frequency	150–250 Hz	250–350 Hz	350–450 Hz

where p_0 is the sound pressure at the sound point when the sound barrier is not placed.

5.1 | Example 1

In the first example, the acoustic performance of three different rigid sound barriers is analyzed. The sound barrier is placed on a rigid ground with the cross-section shown in Figure 5. The specific size parameters of the sound barrier are shown in Figure 6. The boundary of the vertical sound barrier, the Half-Y-shaped sound barrier, and the T-shaped sound barrier are discretized into 2496, 2586, and 2892 boundary points, respectively.

The accuracy and validity of BM-SBM are established by introducing FEM. In FEM, the domain is enclosed by a rectangle $[-1, 9] \times [0, 5]$ with a perfectly matched layer (PML) of thickness 1 m. Figure 7 shows the SPLs at the point (5, 1.5) under different frequencies obtained using BM-SBM and FEM. It is noteworthy that BM-SBM converges by requiring fewer nodes, while FEM requires more elements. As an infinite-field problem, FEM needs to discretize the whole domain including PML, while BM-SBM only needs to discretize the boundary and ensures high computational accuracy due to the use of fundamental solutions. Subsequently, the computational domain of interest is discretized into 30 356 elements, including 898 boundary elements and 26 994 domain elements. The distribution of SPL around the vertical sound barrier predicted by BM-SBM and FEM at different
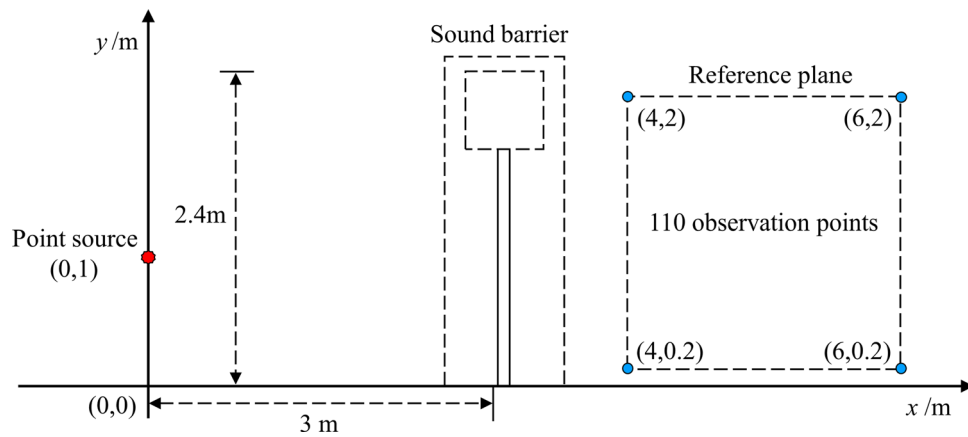
FIGURE 5 Cross-section of the sound barrier.
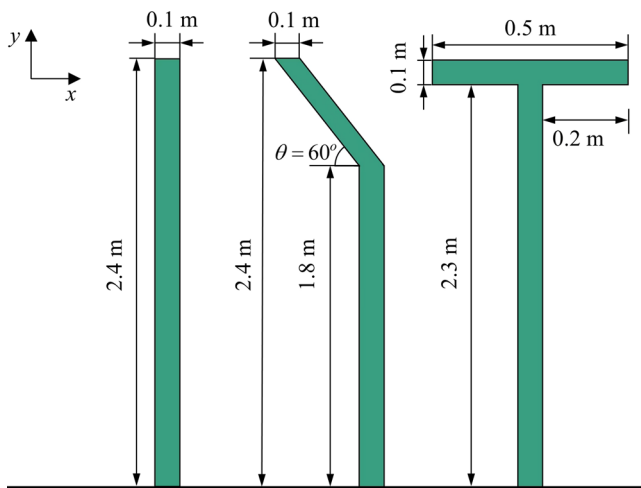
FIGURE 6 Size parameters of sound barriers with different shapes.

frequencies and their relative errors are shown in Figure 8. The numerical results obtained using BM-SBM demonstrate excellent agreement with those obtained using FEM. Subsequently, we use BM-SBM to predict the distribution of SPL around the Half-Y-shaped and T-shaped sound barriers at different frequencies (Figures 9 and 10). It can be seen that the SPL behind the T-shaped sound barrier is smaller than that behind the other two sound barriers.

Afterward, the rigid sound barrier is covered with sound-absorbing material. The 110 uniformly distributed points on the reference plane are selected as observation points (Figure 5). The average values of SPL at 110 observation points corresponding to different admittance values at 200, 300, and 400 Hz frequencies are calculated. The influence curves of the admittance value of the sound-absorbing material on the noise reduction effect of the sound barrier are shown in Figure 11. A higher admittance value can improve the noise reduction effect of the sound barrier. The T-shaped sound barrier with sound-absorbing materials has better

efficiency. To sum up, the T-shaped sound barrier performs best whether it is covered with sound-absorbing materials or not.

5.2 | Example 2

In the second example, the impact of sound-absorbing material distribution on the acoustic performance of the sound barrier is studied. For testing purposes, sound-absorbing materials with an admittance value of 1 are selected. Five different cases are considered based on various combinations of covered and uncovered sound-absorbing materials on the left boundary of the vertical sound barrier, as illustrated in Figure 12. Two reference lines are chosen to calculate the insertion loss. The first reference line is a horizontal line positioned at a height of 1.5 m above the ground. It extends from the sound barrier to a location 40 m behind the sound barrier. The second reference line is a vertical straight line positioned 15 m behind the sound barrier. It spans from the ground to a height of 10 m above the ground.

Figures 13–15 show the insertion loss curves for different cases at different frequencies. It can be seen that the trends of insertion loss in the five cases are basically the same. The negative values of insertion loss result from the interference phenomenon with other sound waves after the reflection of diffracted sound waves in contact with the ground. Case 2 only needs half of the volume of Case 5 to achieve the same effect as Case 5, and the insertion loss even surpasses that of Case 5 at some frequencies and locations, which means that complete sound-absorbing material coverage is not optimal. It is worth noting that the insertion loss of Case 1 is not the lowest. The above findings demonstrate the need for optimal design of the sound-absorbing material distribution on the sound barrier. This conclusion was previously reached also in Ref. 13.
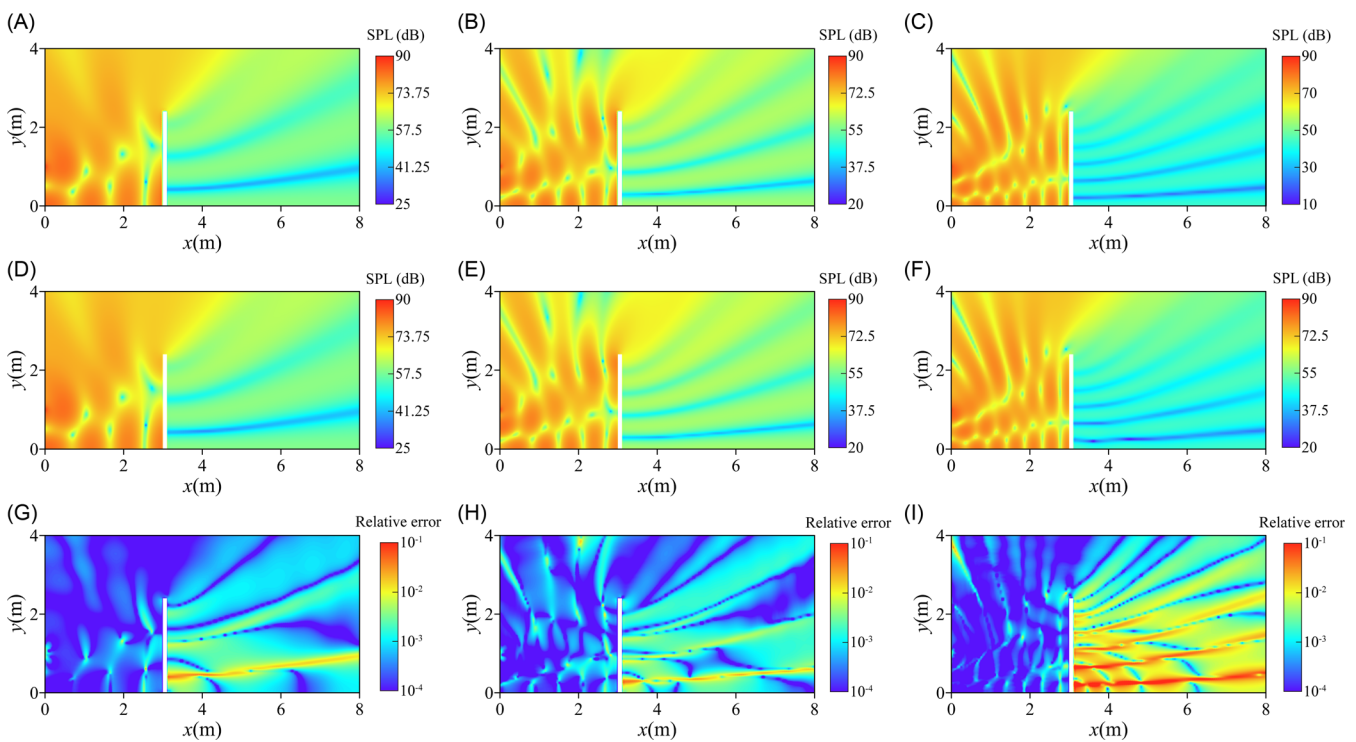
5.3 | Example 3

In the last example, the distribution of sound-absorbing materials on the surface of the sound barrier is optimized to verify the effectiveness and

WILEY |
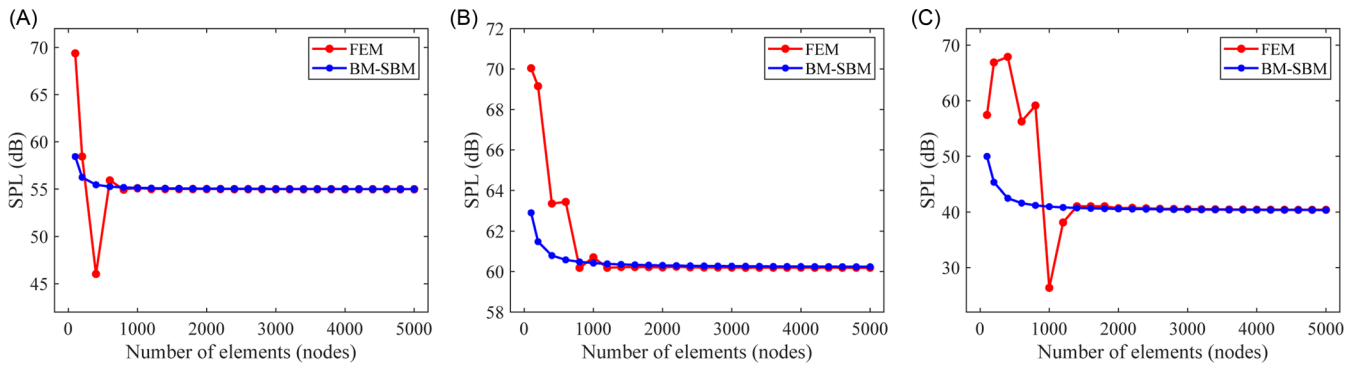
FIGURE 7 Sound pressure level at (5, 1.5) for different numbers of elements and nodes: (A) $f = 200$ Hz, (B) $f = 300$ Hz, and (C) $f = 400$ Hz. BM-SBM, Burton–Miller-type singular boundary method; FEM, finite element method.

FIGURE 8 Distributions of SPL around the vertical sound barrier at different frequencies: (A) Results obtained by FEM ($f = 200$ Hz), (B) results obtained by FEM ($f = 300$ Hz), (C) results obtained by FEM ($f = 400$ Hz), (D) results obtained by BM-SBM ($f = 200$ Hz), (E) results obtained by BM-SBM ($f = 300$ Hz), (F) results obtained by BM-SBM ($f = 400$ Hz), (G) relative error of the two methods ($f = 200$ Hz), (H) relative error of the two methods ($f = 300$ Hz), (I) relative error of the two methods ($f = 400$ Hz). BM-SBM, Burton–Miller-type singular boundary method; FEM, finite element method; SPL, sound pressure level.
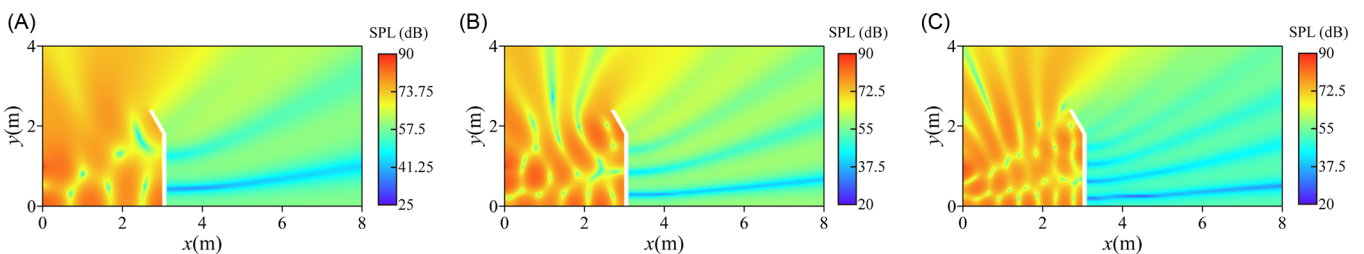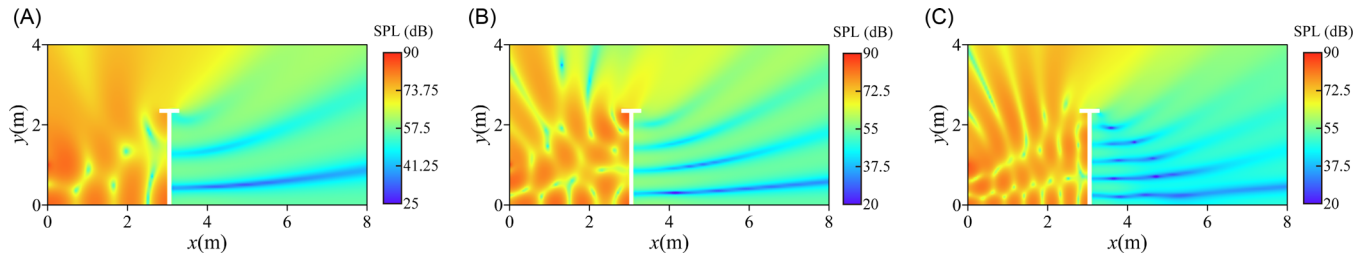

FIGURE 9 Distributions of SPL around the Half-Y-shaped sound barrier at different frequencies: (A) $f = 200$ Hz, (B) $f = 300$ Hz, and (C) $f = 400$ Hz. SPL, sound pressure level.

applicability of the proposed method. The sound barrier is placed on a rigid ground with the cross-section shown in Figure 5. The specific size parameters of the sound barrier are shown in Figure 6. Sound-absorbing material with an admittance value of 1 is selected for the test. The 110 observation points uniformly distributed on the observation plane are selected and the sound pressure values at these points are used as the objective function for optimization. The convergence parameters τ and the initial value of the design variable ρ_i (i = 1, 2, ..., N_e) are set to 10^{-5} and 1, respectively.
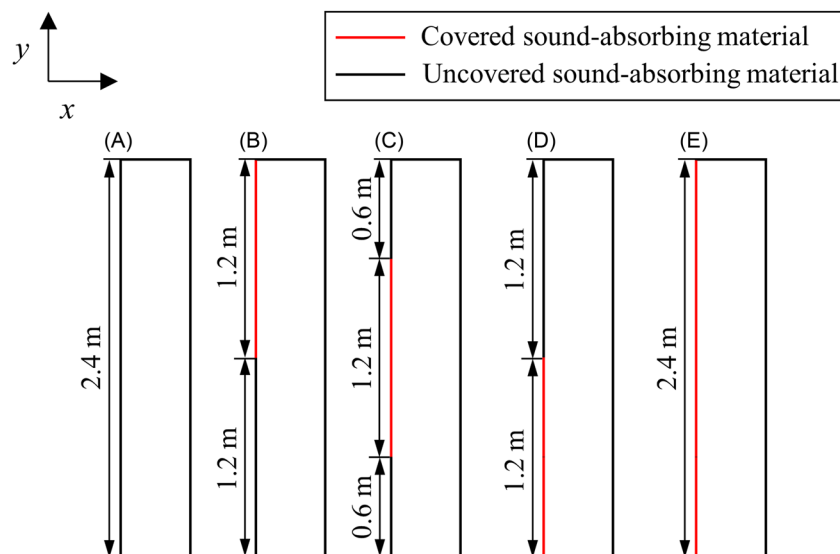
First, the distribution of sound-absorbing materials on the surface is optimized for three shapes at a frequency of 200 Hz. The volume ratio constraint ξ is set to 1. Figure 16 shows the

FIGURE 10 Distributions of SPL around the T-shaped sound barrier at different frequencies: (A) f = 200 Hz, (B) f = 300 Hz, and (C) f = 400 Hz. SPL, sound pressure level.
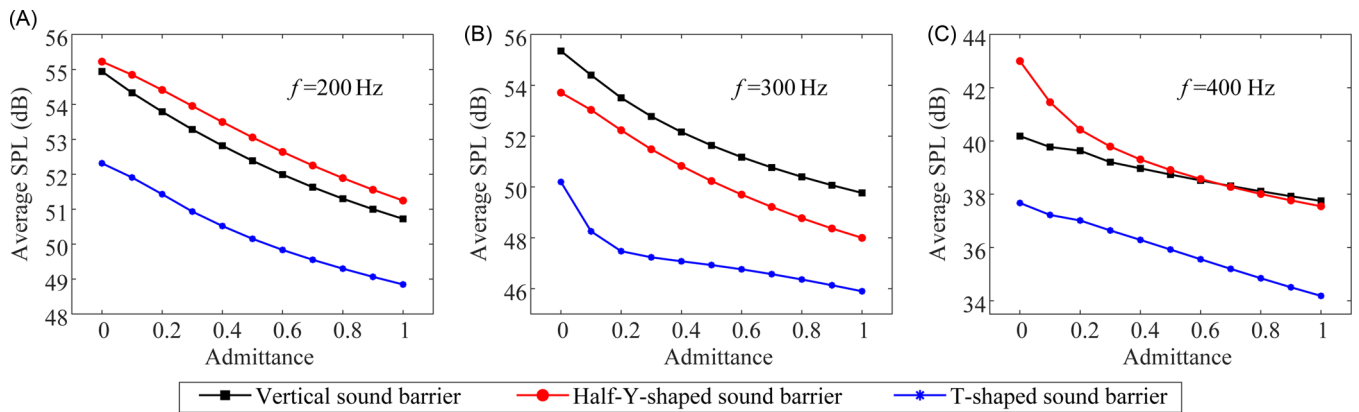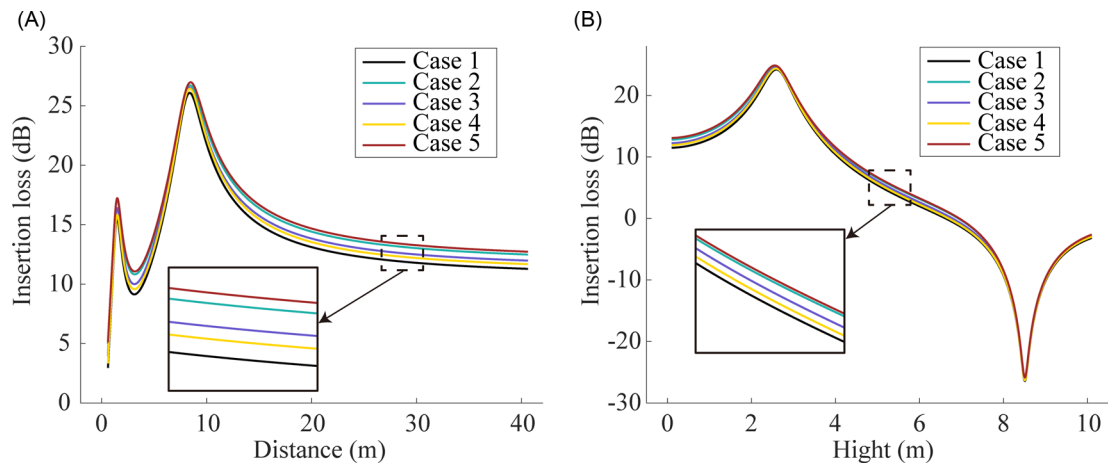

FIGURE 11 Average SPLs at observation points in the reference plane for different values of admittance: (A) f = 200 Hz, (B) f = 300 Hz, and (C) f = 400 Hz.
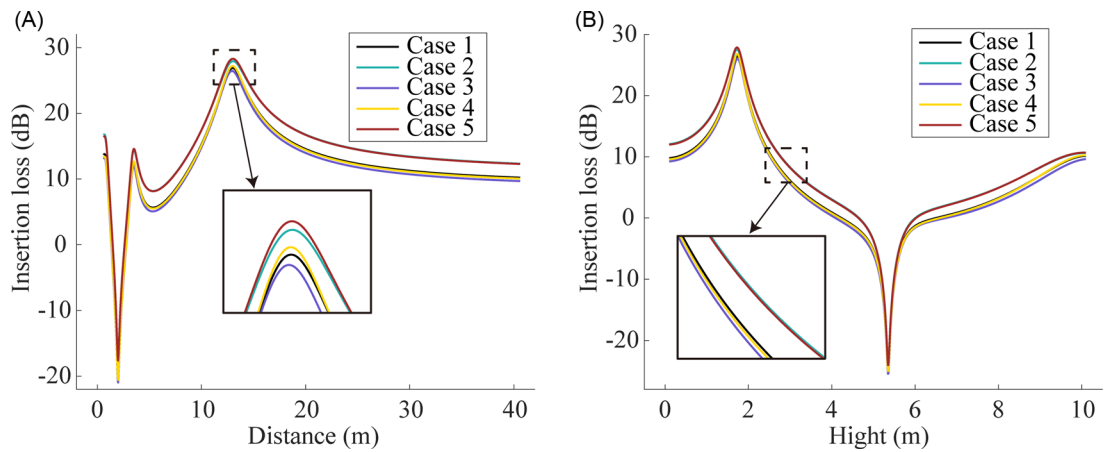

FIGURE 12 Distribution of sound-absorbing materials for sound barriers: (A) Case 1, (B) Case 2, (C) Case 3, (D) Case 4, (E) Case 5.
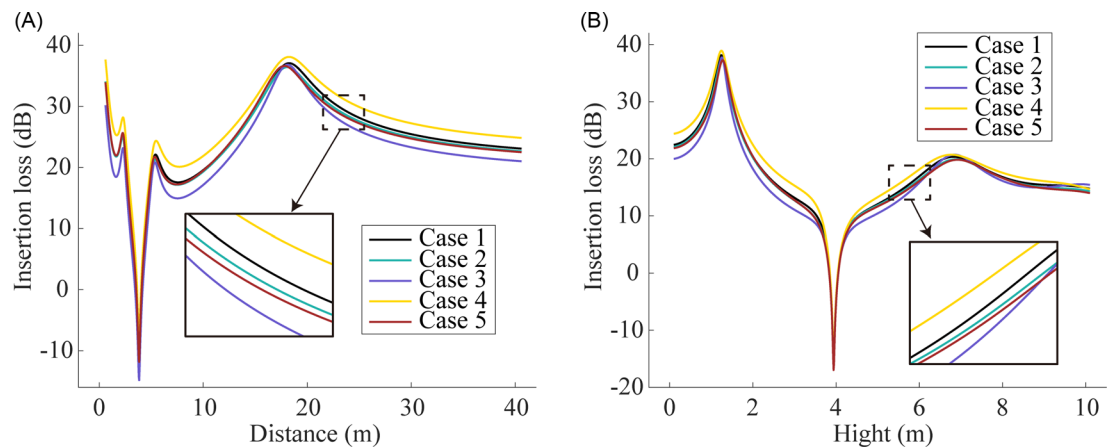
FIGURE 13 Insertion loss curves of the sound barrier under different locations ($f = 200$ Hz): (A) Insertion loss curve at the height of 1.5 m above the ground in the horizontal direction. (B) Insertion loss curve in the vertical direction at a distance of 15 m from the sound barrier.

FIGURE 14 Insertion loss curves of the sound barrier under different locations ($f = 300$ Hz): (A) Insertion loss curve at the height of 1.5 m above the ground in the horizontal direction. (B) Insertion loss curve in the vertical direction at a distance of 15 m from the sound barrier.

FIGURE 15 Insertion loss curves of the sound barrier under different locations ($f = 400$ Hz): (A) Insertion loss curve at the height of 1.5 m above the ground in the horizontal direction. (B) Insertion loss curve in the vertical direction at a distance of 15 m from the sound barrier.

optimal distribution of sound-absorbing materials for the three sound barrier surfaces. Figure 17 shows the iterative history of the objective function and the volume ratio. It can be seen that the optimized volume ratio of all three sound barriers is less than 1. This also confirms our previous conclusion that the noise reduction effect of full-coverage sound-absorbing materials is not necessarily optimal.

The engineering application is more concerned with optimal design under the premise that the design material is restricted. Therefore, the volume constraint ratio is set to 0.5 for optimization. Figures 18–20 show the optimal distribution of sound-absorbing materials on the surface of the vertical sound barrier, the half-Y sound barrier, and the T-shaped sound barrier at different frequencies, respectively. Figure 21 shows the iterative history of the corresponding objective function. Table 2 shows the average SPLs of the rigid, full sound-absorbing material and the optimized sound

barrier at the observation points within the reference plane. The above results confirm the feasibility and effectiveness of the optimization method proposed in this paper.

There exists a dependence on both frequency and shape for the optimization problem. In real life, sound barriers are not exposed to a specific sound frequency only. Therefore, we define a new objective function to study the optimization of the frequency range. The new objective function can be expressed as

$$\Pi_{new} = \frac{1}{\omega_2 - \omega_1} \int_{\omega_1}^{\omega_2} \Pi d\omega, \tag{28}$$

where ω_1 and ω_2 denote the lower and upper limits of the frequency range, respectively. In this example, we consider a frequency range of 200–500 Hz. The volume constraint ratio is set to 0.5. Figure 22 shows the corresponding optimization results for different sound barriers in this frequency range.
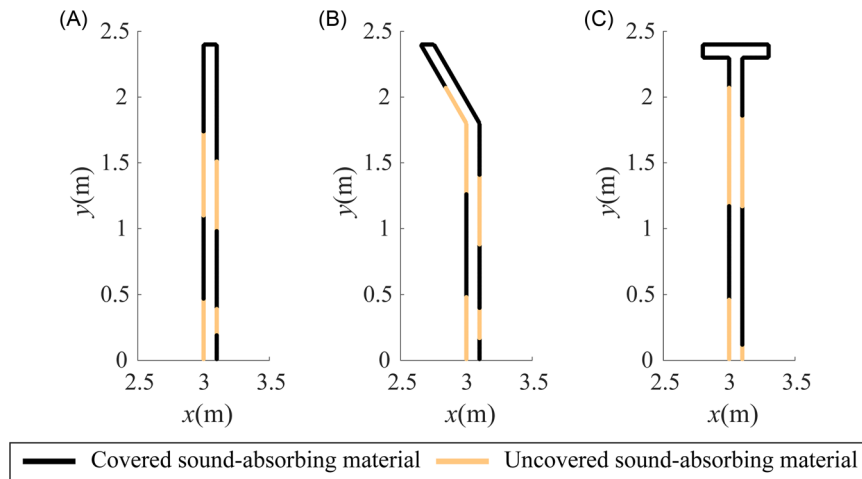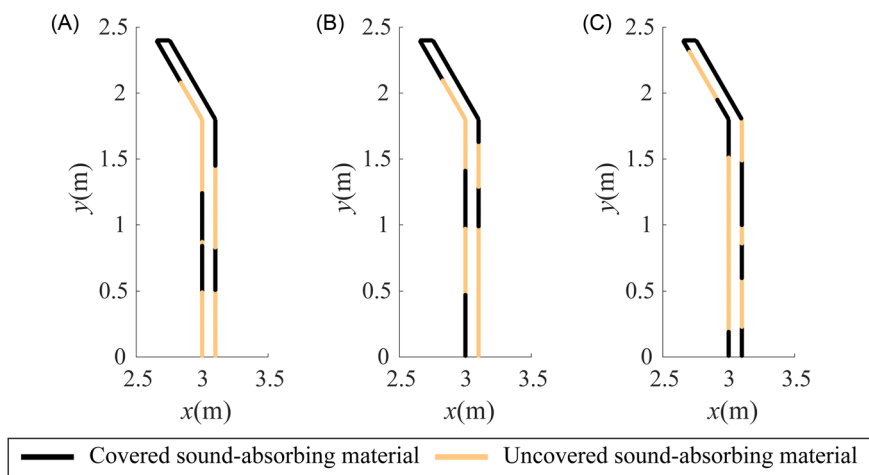

FIGURE 16 Optimal distribution of sound-absorbing materials on the surface of different sound barriers at a frequency of 200 Hz: (A) vertical sound barrier, (B) half-Y-shaped sound barrier, and (C) T-shaped sound barrier.
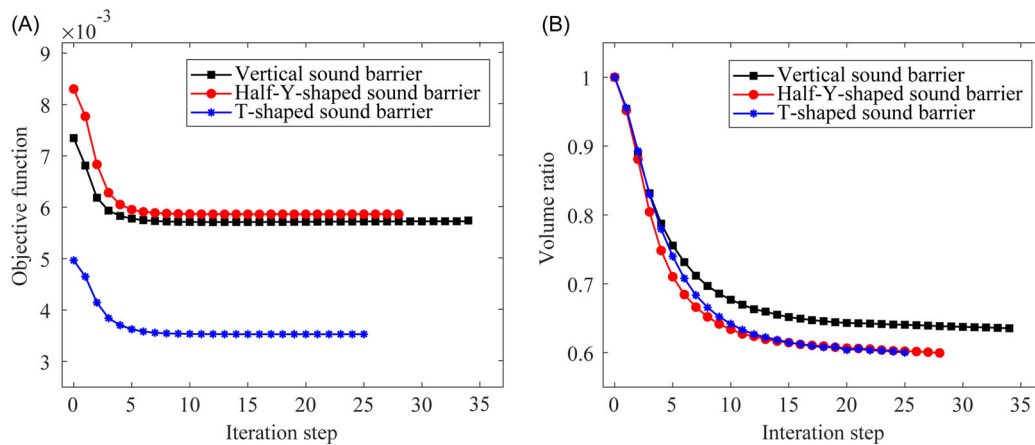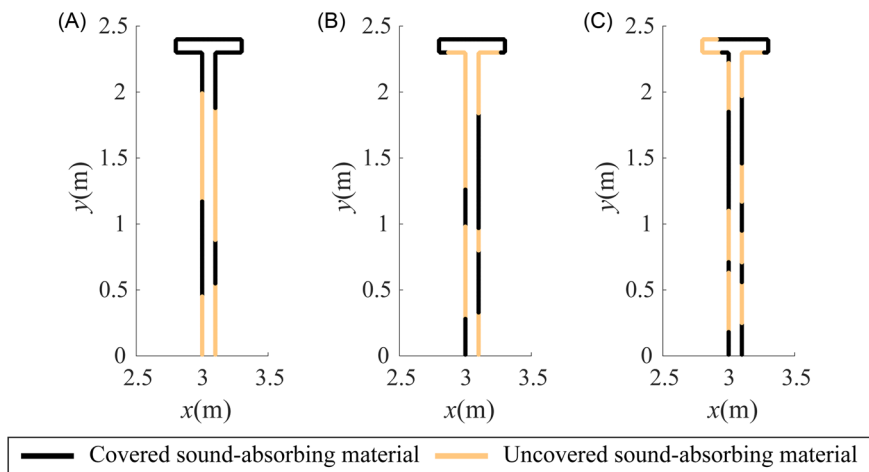

FIGURE 17 Iterative history of the objective function and volume ratio at a frequency of 200 Hz: (A) Iterative history of the objective function. (B) Iterative history of the volume ratio.
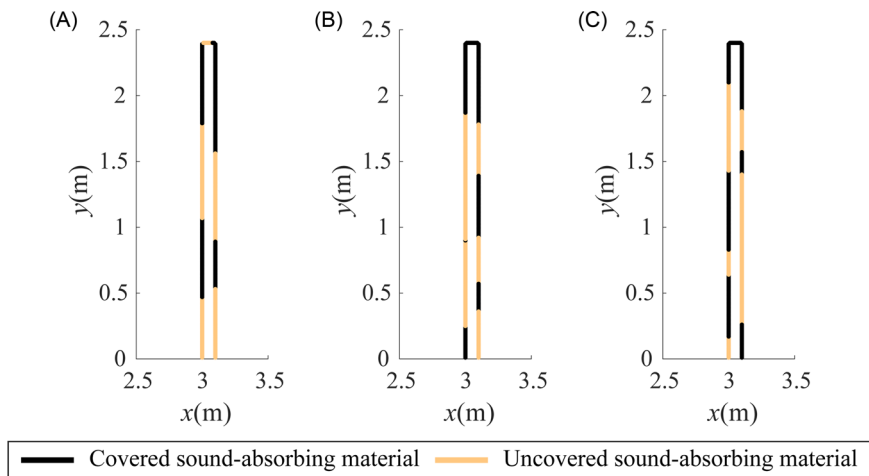
FIGURE 18 Optimal distribution of sound-absorbing materials on the surface of vertical sound barriers at different frequencies: (A) 200 Hz, (B) 300 Hz, and (C) 400 Hz.

FIGURE 19 Optimal distribution of sound-absorbing materials on the surface of Half-Y-shaped sound barriers at different frequencies: (A) 200 Hz, (B) 300 Hz, and (C) 400 Hz.
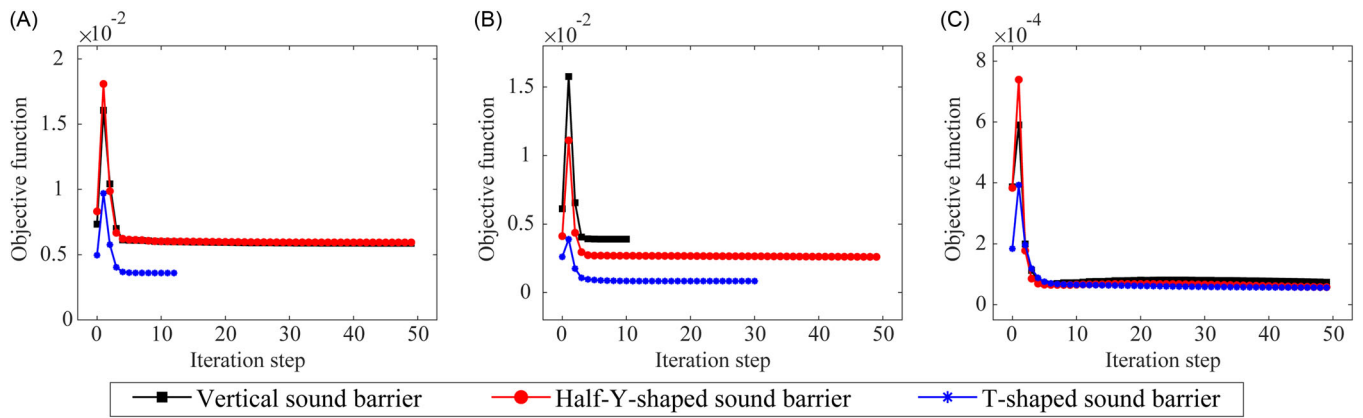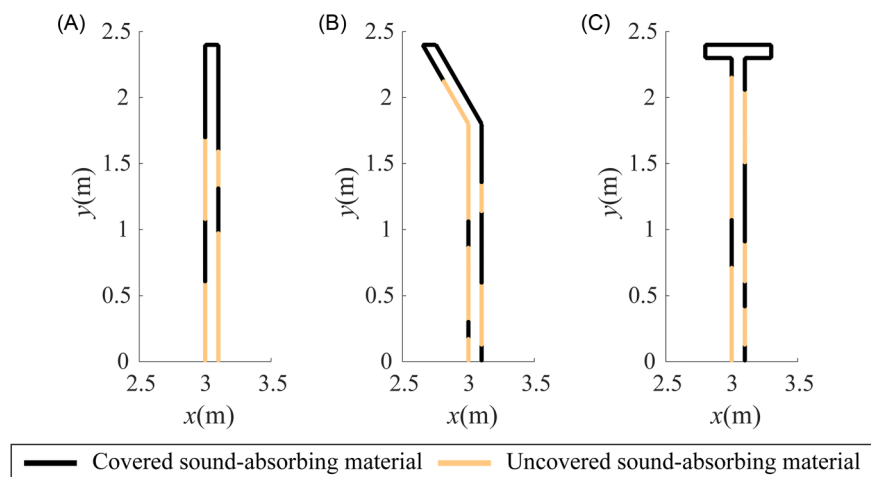

FIGURE 20 Optimal distribution of sound-absorbing materials on the surface of T-shaped sound barriers at different frequencies: (A) 200 Hz, (B) 300 Hz, and (C) 400 Hz.

FIGURE 21 Iteration history of the objective function at different frequencies: (A) 200 Hz, (B) 300 Hz, and (C) 400 Hz.

TABLE 2 Average SPLs at observation points in the reference plane corresponding to sound barriers with different material distributions.

Frequency (Hz)	Sound barrier	Material distribution		
		Full rigid (dB)	Full sound-absorbing material (dB)	Optimal design (dB)
200	Vertical	55.14	50.75	49.60
	Half-Y-shaped	55.45	51.29	49.65
	T-shaped	52.67	48.97	47.59
300	Vertical	55.59	49.80	47.99
	Half-Y-shaped	53.76	48.04	46.04
	T-shaped	50.29	46.04	41.52
400	Vertical	40.64	37.81	30.35
	Half-Y-shaped	43.11	37.55	29.99
	T-shaped	39.14	34.35	28.78

FIGURE 22 Optimal distributions of sound-absorbing materials on the surface of the sound barriers in a frequency range (200–500 Hz).

6 | CONCLUSIONS

In this paper, the acoustic performance of sound barriers with different shapes is analyzed by BM-SBM, and the distribution of sound-absorbing materials on the sound barrier surface is optimized by BM-SBM and the SIMP method. The penalization parameter and the smoothed Heaviside function are introduced to achieve a continuous decrease in the proportion of structural intermediate-density units during the iterative optimization process. Numerical results demonstrate the feasibility and effectiveness of the proposed method. The simulation results reveal that the T-shaped sound barrier is found to be the most effective sound barrier and the noise reduction effect is not necessarily the best if the entire surface of the sound barrier is covered with sound-absorbing materials. Although this paper only analyzes and optimizes 2D sound barriers, the framework can also be applied to 3D sound barriers.

CONFLICT OF INTEREST STATEMENT

The authors declare no conflict of interest.

DATA AVAILABILITY STATEMENT

The data that support the findings of this study are available from the corresponding author upon reasonable request.

ORCID

Hanqing Liu http://orcid.org/0009-0003-4000-3652
Fajie Wang http://orcid.org/0000-0002-5162-1099

REFERENCES

1. May DN, Osman NM. Highway noise barriers: new shapes. *J Sound Vib*. 1980;71(1):73-101.
2. Joynt JLR, Kang J. The influence of preconceptions on perceived sound reduction by environmental noise barriers. *Sci Total Environ*. 2010;408(20):4368-4375.
3. Hong JY, Jeon JY. The effects of audio-visual factors on perceptions of environmental noise barrier performance. *Landsc Urban Plan*. 2014;125:28-37.
4. Reiter P, Wehr R, Ziegelwanger H. Simulation and measurement of noise barrier sound-reflection properties. *Appl Acoust*. 2017;123:133-142.
5. Papadakis NM, Stavroulakis GE. Finite element method for the estimation of insertion loss of noise barriers: comparison with various formulae (2D). *Urban Sci*. 2020;4(4):77.
6. Monazzam MR, Abbasi M, Yazdanirad S. Performance evaluation of T-shaped noise barriers covered with oblique diffusers using boundary element method. *Archiv Acoust*. 2019;44:521-531.
7. Lam YW. A boundary element method for the calculation of noise barrier insertion loss in the presence of atmospheric turbulence. *Appl Acoust*. 2004;65(6):583-603.
8. Grubeša S, Suhanek M, Đurek I, Petošić A. Combined acoustical and economical noise barrier optimization using genetic algorithms. *Gradevinar*. 2019;71:177-185.
9. Liu C, Chen L, Zhao W, Chen H. Shape optimization of sound barrier using an isogeometric fast multipole boundary element method in two dimensions. *Eng Anal Bound Elem*. 2017;85:142-157.
10. Chen L, Liu C, Zhao W, Liu L. An isogeometric approach of two dimensional acoustic design sensitivity analysis and topology optimization analysis for absorbing material distribution. *Comput Methods Appl Mech Eng*. 2018;336:507-532.
11. Desai J, Faure A, Michailidis G, Parry G, Estevez R. Topology optimization in acoustics and elasto-acoustics via a level-set method. *J Sound Vib*. 2018;420:73-103.
12. Kim KH, Yoon GH. Optimal rigid and porous material distributions for noise barrier by acoustic topology optimization. *J Sound Vib*. 2015;339:123-142.
13. Zhao W, Chen L, Zheng C, Liu C, Chen H. Design of absorbing material distribution for sound barrier using topology optimization. *Struct Multidisciplin Optim*. 2017;56:315-329.
14. Chen L, Zhao W, Yuan X, Zhou B. Study on the optimization of the distribution of absorbing material on a noise barrier. *Acoust Austral*. 2018;46:119-130.
15. Gu Y, Fu Z, Golub MV. A localized Fourier collocation method for 2D and 3D elliptic partial differential equations: theory and MATLAB code. *Int J Mech Syst Dynam*. 2022;2(4):339-351.
16. Wei X, Luo W. 2.5D singular boundary method for acoustic wave propagation. *Appl Math Lett*. 2021;112:106760.
17. Chen Z, Wang F, Cheng S, Wu G. Localized MFS for three-dimensional acoustic inverse problems on complicated domains. *Int J Mech Syst Dynam*. 2022;2(1):143-152.
18. Sun L, Fu Z, Chen Z. A localized collocation solver based on fundamental solutions for 3D time harmonic elastic wave propagation analysis. *Appl Math Computat*. 2023;439:127600.
19. Ju B, Qu W. Three-dimensional application of the meshless generalized finite difference method for solving the extended Fisher–Kolmogorov equation. *Appl Math Lett*. 2023;136:108458.
20. Zhang Y, Dang S, Li W, Chai Y. Performance of the radial point interpolation method (RPIM) with implicit time integration scheme for transient wave propagation dynamics. *Comput Math Appl*. 2022;114:95-111.
21. Chen Z, Sun L. A boundary meshless method for dynamic coupled thermoelasticity problems. *Appl Math Lett*. 2022;134:108305.
22. Li Y, Liu C, Li W, Chai Y. Numerical investigation of the element-free galerkin method (EFGM) with appropriate temporal discretization techniques for transient wave propagation problems. *Appl Math Computat*. 2023;442:127755.
23. Gu Y, Lin J, Fan C-M. Electroelastic analysis of two-dimensional piezoelectric structures by the localized method of fundamental solutions. *Adv Appl Math Mech*. 2023;15(4):880-900.
24. Qiu L, Ma X, Qin Q-H. A novel meshfree method based on spatio-temporal homogenization functions for one-dimensional fourth-order fractional diffusion-wave equations. *Appl Math Lett*. 2023;142:108657.
25. Liu GR. *Meshfree Methods: Moving Beyond the Finite Element Method*. 2nd ed. CRC Press; 2018.
26. Fu Z, Xi Q, Gu Y, et al. Singular boundary method: a review and computer implementation aspects. *Eng Anal Bound Elem*. 2023;147:231-266.
27. Griebel M, Schweitzer MA. *Meshfree Methods for Partial Differential Equations VIII*. Springer International Publishing; 2017.
28. Fu Z-J, Chen W, Gu Y. Burton–Miller-type singular boundary method for acoustic radiation and scattering. *J Sound Vib*. 2014;333(16):3776-3793.

29. Li W, Wang F. Precorrected-FFT accelerated singular boundary method for high-frequency acoustic radiation and scattering. *Mathematics*. 2022;10(2):238.

30. Lan L, Cheng S, Sun X, Li W, Yang C, Wang F. A fast singular boundary method for the acoustic design sensitivity analysis of arbitrary two-and three-dimensional structures. *Mathematics*. 2022; 10(20):3817.

31. Cheng S, Wang F, Li P-W, Qu W. Singular boundary method for 2D and 3D acoustic design sensitivity analysis. *Comput Math Appl*. 2022; 119:371-386.

32. Fakhraei J, Arcos R, Pàmies T, Liravi H, Romeu J. Modified 2.5D singular boundary methods to deal with spurious eigensolutions in exterior acoustic problems. *J Sound Vib*. 2023;550:117597.

33. Svanberg K. The method of moving asymptotes—a new method for structural optimization. *Int J Numer Meth Eng*. 1987;24(2): 359-373.

34. Wang Y, Li X, Long K, Wei P. Open-source codes of topology optimization: a summary for beginners to start their research. *CMES-Comput Model Eng Sci*. 2023;131(1):1-34.

35. Xu S, Cai Y, Cheng G. Volume preserving nonlinear density filter based on heaviside functions. *Struct Multidisciplin Optim*. 2010;41: 495-505.

36. Cheng S, Wang F, Wu G, Zhang C. A semi-analytical and boundary-type meshless method with adjoint variable formulation for acoustic design sensitivity analysis. *Appl Math Lett*. 2022;131:108068.

37. Yu L. *Progress on Noise Reduction in Road Traffic Environment from 2000*. Atlantis Press; 2022:184-189.

AUTHOR BIOGRAPHIES

Hanqing Liu is currently a postgraduate student at the College of Mechanical and Electrical Engineering, Qingdao University, China. His research focuses on vibration and noise control.

Fajie Wang received his PhD degree in fluid mechanics from Hohai University in 2018. He is currently a professor at the College of Mechanical and Electrical Engineering, Qingdao University, China. His research interests focus on computational mechanics, machine learning, optimum structural design, and fractal and fractional modeling.

Chuanzeng Zhang is a professor and chair of Structural Mechanics, the Department of Civil Engineering, School of Science and Technology, University of Siegen, Germany. He received his Diploma (Dipl.-Ing.) in 1983 and his PhD (Dr.-Ing.) in 1986 from Technical University Darmstadt, Germany. Before his appointment at the University of Siegen in 2004, he was an associate professor and professor at Tongji University in Shanghai, China, and a professor at the University of Applied Sciences Zittau/Görlitz, Germany. His research interests include computational mechanics, structural mechanics, fracture and damage mechanics, and acoustics. He is an adjunct/guest/consulting professor at five universities and an Honorary professor at four universities. He is a member of the European Academy of Sciences, the European Academy of Sciences and Arts, and Academia Europaea.